Chinese Chemical Letters 31 (2020) 1034–1038

Contents lists available at ScienceDirect

Chinese Chemical Letters

journal homepage: www.elsevier.com/locate/cclet

Communication

Additive-free porous assemblies of $Ti_3C_2T_x$ by freeze-drying for high performance supercapacitors

Yue Yang[a], Lili Wu[a,b,*], Lu Li[a], Shuangyan Lin[a], Lina Bai[a], Xinzhi Ma[a], Zhitao Shao[a], Xitian Zhang[a,*]

[a] Key Laboratory for Photonic and Electronic Bandgap Materials, Ministry of Education, School of Physics and Electronic Engineering, Harbin Normal University, Harbin 150025, China

[b] Center for Engineering Training and Basic Experimentation, Heilongjiang University of Science and Technology, Harbin 150022, China

ARTICLE INFO

Article history:
Received 23 December 2019
Received in revised form 5 February 2020
Accepted 7 March 2020
Available online 14 February 2020

Keywords:
MXenes
$Ti_3C_2T_x$
Supercapacitor
Freeze-drying
Additive-free

ABSTRACT

$Ti_3C_2T_x$ has shown great potential in energy storage filed, but the restacking between $Ti_3C_2T_x$ nanosheets seriously hampers the maximization of its capacitance. In this study, we rationally designed and synthesized porous $Ti_3C_2T_x$ assemblies without any additive by introducing ice as spacers using a facile freeze-drying method. The porous $Ti_3C_2T_x$ assemblies have a three-dimensional network structure, which consists of ultra large $Ti_3C_2T_x$ lamellar walls and lots of macro- and mesopores. It has been proven that there are more -O groups on the surface of the porous $Ti_3C_2T_x$ assemblies than the $Ti_3C_2T_x$ film. The porous $Ti_3C_2T_x$ assemblies deliver a maximum areal capacitance of 1668 mF/cm^2 when the mass loading is 8.4 mg/cm^2, an optimized specific capacitance of 247.2 F/g when the mass loading is 5.3 mg/cm^2, and 87% capacitance retention over 10000 cycles. The symmetric solid-state supercapacitors based on the porous $Ti_3C_2T_x$ assemblies show an areal capacitance of 355.8 mF/cm^2, the maximum power density of 50 mW/cm^2 and an outstanding flexibility under different deformation.

With the increase of energy requirement, most researchers pay more attention to the development of energy storage devices. Compared with lithium-ion batteries [1,2] and lithium-sulfur batteries [3,4], supercapacitors [5–7] are widely concerned because of high power density and long cycling life. Furthermore, mechanical flexibility is another important consideration for portable and wearable energy-storage devices. The flexible solid-state supercapacitors have been extensively explored [8,9], including sandwich-type solid state supercapactiors [10], fiber-shaped supercapactiors [11] and microsupercapacitors [12–14]. It is worth noting that the electrode material is critical. Therefore, various functional electrode materials, such as carbon materials [15] and metal oxides [16,17], have been developed. However, it is a challenge to find flexible electrode materials with excellent mechanical properties and high capacitance simultaneously.

In recent years, an emerging family of layered early transition metal carbides and/or nitrides, MXenes, was discovered in 2011 [18]. MXenes can be produced by etching the “A” layers from the MAX phases. Among the MXenes family, $Ti_3C_2T_x$ is considered as a promising electrode material because of excellent conductivity, high areal capacitance and mechanical flexibility, exhibiting great advantage in the field of energy storage equipment [19–21], especially for supercapacitors [22–25]. However, the irreversible restacking between $Ti_3C_2T_x$ nanosheets, just like graphene, is inevitable. It is because the strong van der Waals interaction between adjacent $Ti_3C_2T_x$ nanosheets [24]. The irreversible restacking results in a significant decline of accessible surface area and seriously hinders electrochemical performance. It is well known that the establishment of three-dimensional porous structures has been successfully applied to graphene to alleviate the restacking [26]. By referring to graphene, researchers have prepared $Ti_3C_2T_x$ aerogels with the help of ethyl-enediamine (EDA), or thiourea dioxide and ammonia solution [21,27]. However, some of these additives might not be beneficial to high electrochemical performance. For example, the introduction of EDA reduced the cycle stability of the $Ti_3C_2T_x$ electrode, and partially removed the termination of O, which should be an essential participant in electrochemical reaction in the H_2SO_4 electrolyte following Eq. S1 (Supporting information) [27,28]. In this work, we rationally designed and synthesized porous $Ti_3C_2T_x$ assemblies without any additive by introducing ice as spacers by a

---

[*] Corresponding authors at: Key Laboratory for Photonic and Electronic Bandgap Materials, Ministry of Education, School of Physics and Electronic Engineering, Harbin Normal University, Harbin 150025, China.

E-mail addresses: wll790107@hotmail.com (L. Wu), xtzhangzhang@hotmail.com (X. Zhang).

https://doi.org/10.1016/j.cclet.2020.02.027

facile frozen-drying method. On the one hand, the ice spacers crystallized from the aqueous $Ti_3C_2T_x$ colloidal suspension could partially prevent the nanosheets from restacking. On the other hand, the ice crystallization in the freeze-drying process might provide an opportunity to tailor the chemistry and properties of $Ti_3C_2T_x$ and improve their performances in electrochemical applications. This method is also applied to other 2D materials beyond MXene in the field of energy storage and expected to enhance their electrochemical performances [9,29,30].

Fig. S1 (Supporting information) demonstrates the fabrication of porous $Ti_3C_2T_x$ assemblies. The morphology of the porous $Ti_3C_2T_x$ assemblies was investigated by SEM. As shown in Fig. 1a, it is quite uniform with low magnification, and the $Ti_3C_2T_x$ assemblies have a three-dimensional porous network structure composed of ultra large $Ti_3C_2T_x$ lamellar walls and lots of macropores with appropriate porous size of tens of micrometers. Fig. S2 (Supporting information) suggests that there are lots of mesopores in the $Ti_3C_2T_x$ assemblies. The pore-size dominantly distributes around 4 nm. The specific surface area of the porous $Ti_3C_2T_x$ assemblies is calculated to be 22.0 m^2/g. Fig. 1b presents the faintly wrinkled surface of the $Ti_3C_2T_x$ lamellar walls, which may induce the generation of mesopores. The lateral size of the lamellar walls of macropores is more than one hundred micrometers. It is much larger than the lateral size of the reported $Ti_3C_2T_x$ nanosheets (about 3~5 μm) [13,31]. The ultra large lateral size of the $Ti_3C_2T_x$ lamellas is helpful for making up a three-dimensional porous structure consisting of many macro- and mesopores, which would increase the specific surface area and simultaneously facilitate the infiltration and diffusion of electrolyte ions. The detailed microstructure of the ultra large $Ti_3C_2T_x$ lamellas separated from the porous assemblies was further investigated by TEM (Fig. 1c). The lamella is constructed by continuously cross-linking small $Ti_3C_2T_x$ nanosheets, and can provide many active sites, which is important for practical application of supercapacitors. The selected area electron diffraction pattern was tested along the [000 l] zone axis (inset of Fig. 1d).

The XRD pattern of the porous $Ti_3C_2T_x$ assemblies is shown in Fig. 2a. The most intense peak in the XRD pattern of Ti_3AlC_2 is located at $2\theta = 39^\circ$, while it disappears in the XRD pattern of the porous $Ti_3C_2T_x$ assemblies, implying that the $Ti_3C_2T_x$ has been prepared successfully [27]. According to the characteristic peak of (002) at 6.1°, the interlayer spacing of porous $Ti_3C_2T_x$ assemblies is calculated to be 14.5 Å (Fig. 2b), which is less than that of $Ti_3C_2T_x$ film (15.3 Å). It might be caused by the loss of H_2O between the $Ti_3C_2T_x$ layers in the freeze-drying process. The discrepancy in chemical structure between the porous $Ti_3C_2T_x$ assemblies and the $Ti_3C_2T_x$ film can be reflected by Raman spectrum. To exclude the influence of the exposure time and the amount of the used sample, the Raman spectra in the range of 530−770 cm^{-1} for $Ti_3C_2T_x$ assemblies and $Ti_3C_2T_x$ film are normalized and shown in Figs. 2c and d, respectively. Peak-differentiating and imitating were carried out using PeakFit software. According to previous report, the peak located at 590 cm^{-1} is ascribed to the vibrations of the atoms in $Ti_3C_2O_2$ [28]. In analogy with the case of $Ti_3C_2(OH)_2$, the intensity of $Ti_3C_2O_2$ for the porous $Ti_3C_2T_x$ assemblies is obviously higher than that for $Ti_3C_2T_x$ film, indicating the more -O functional groups contained in the porous $Ti_3C_2T_x$ assemblies [28]. The high-resolution O 1s spectra of the porous $Ti_3C_2T_x$ assemblies and $Ti_3C_2T_x$ film are shown in Figs. 2e and f. The O 1s signal can be deconvoluted into four peaks at 533.5, 532.2, 531.1 and 530.2 eV, corresponding to H_2O, Ti-O-H, Ti-O and TiO_2, respectively. Their proportion determined from the O 1s spectra is shown in Table S1 (Supporting information). The proportion of the functional group of -O for the porous $Ti_3C_2T_x$ assemblies is more than that for the $Ti_3C_2T_x$ film, which reinforces the Raman analysis. The proportion of H_2O for the porous $Ti_3C_2T_x$ assemblies is 10.6%, which is less than that for the $Ti_3C_2T_x$ film (17.2%). It implies that some H_2O molecules intercalated into the interlayers of the porous $Ti_3C_2T_x$ assemblies might be partially removed.

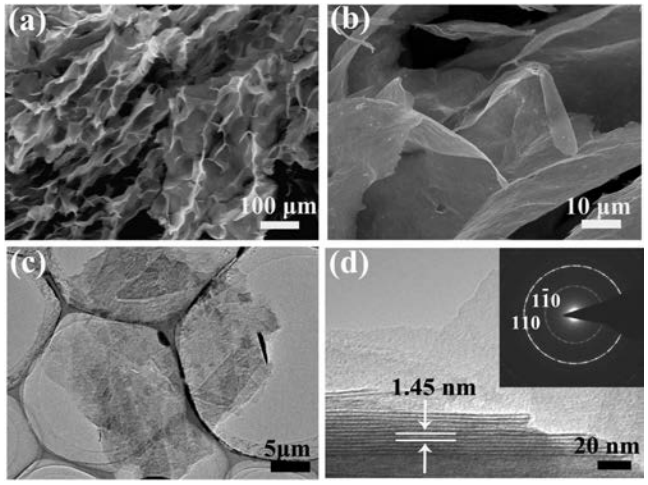

Fig. 1. (a, b) SEM images, (c, d) TEM images of single $Ti_3C_2T_x$ lamella separated from the porous assemblies. Inset is the corresponding selected area electron diffraction pattern.

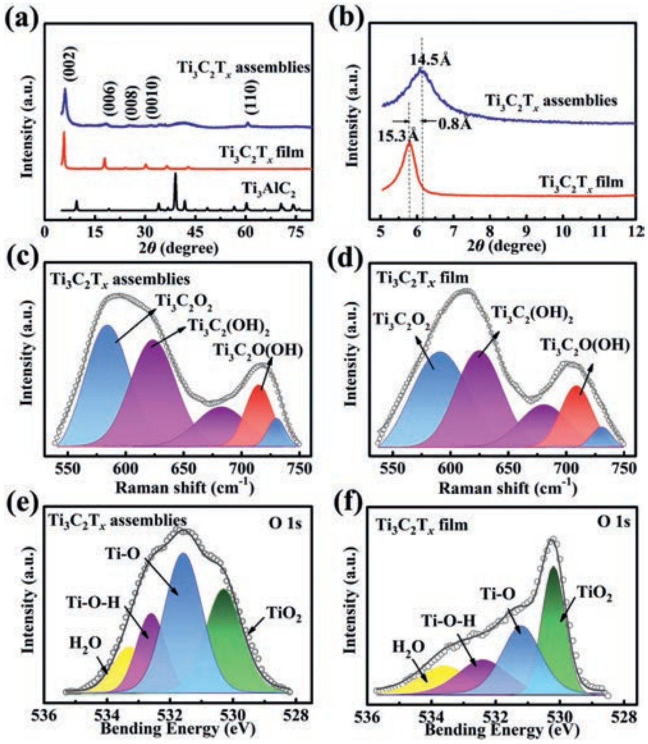

Fig. 2. (a) XRD patterns, (b) Enlarged XRD patterns, (c, d) Raman spectra of porous $Ti_3C_2T_x$ assemblies and $Ti_3C_2T_x$ film. (e, f) O 1s XPS spectra of porous $Ti_3C_2T_x$ assemblies and $Ti_3C_2T_x$ film.

The electrochemical performances of the $Ti_3C_2T_x$ film and porous $Ti_3C_2T_x$ assemblies were firstly studied in a three-electrode configuration by using 1 mol/L H_2SO_4 as electrolyte. Fig. 3a shows the cyclic voltammogram (CV) curves for the porous $Ti_3C_2T_x$ assemblies and $Ti_3C_2T_x$ film with same mass loading at the scan rate of 2 mV/s, besides carbon paper. Compared with porous $Ti_3C_2T_x$ assemblies and $Ti_3C_2T_x$ film, the CV curve for carbon paper is just a straight line. That means the effective capacitive

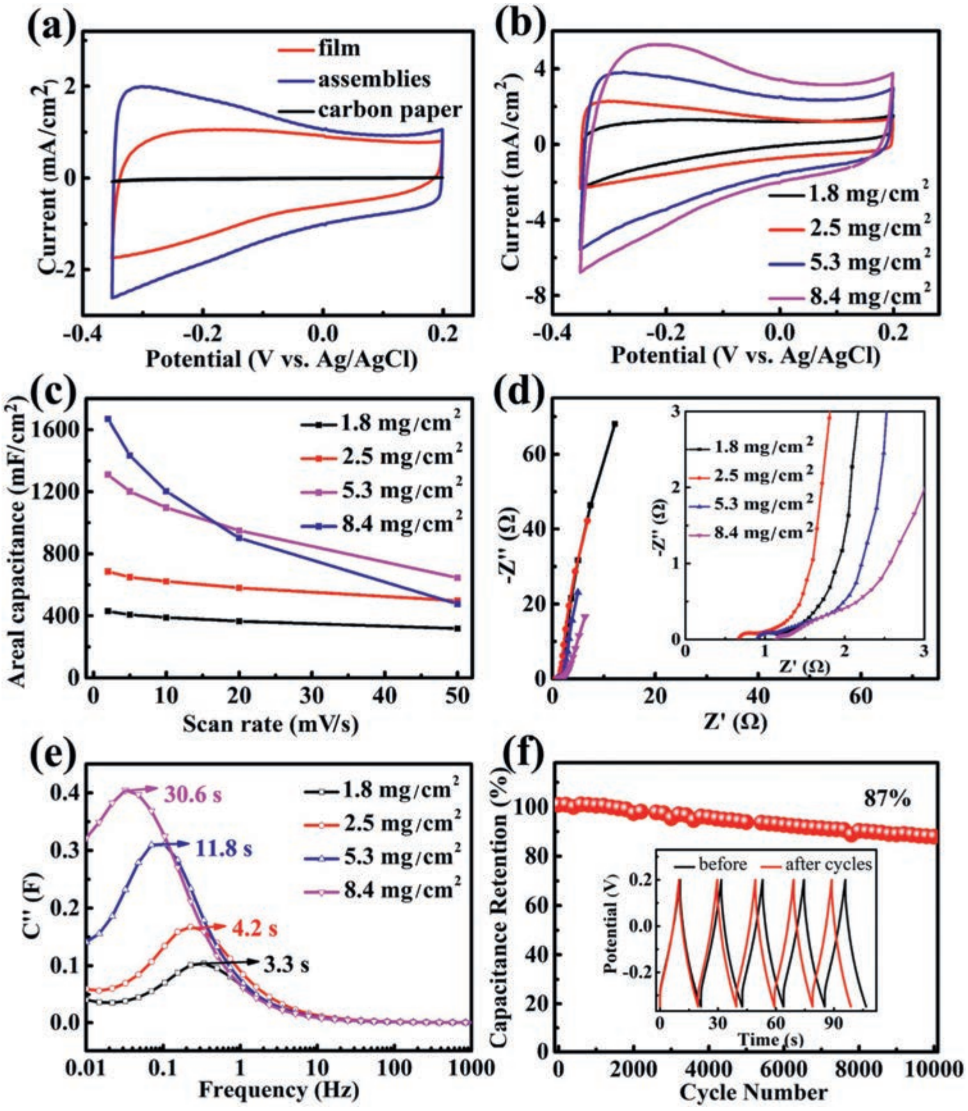

Fig. 3. (a) CV curves of carbon paper, $Ti_3C_2T_x$ film and assemblies. (b) CV curves of $Ti_3C_2T_x$ assemblies. (c) Variation in areal capacitances of $Ti_3C_2T_x$ assemblies with scan rates. (d) Nyquist plots and (e) diffusion time plots of $Ti_3C_2T_x$ assemblies. (f) Cycle stability of $Ti_3C_2T_x$ assemblies, the inset exhibits the GCD curves of before and after 10000 cycles.

contribution from carbon paper compared with that from $Ti_3C_2T_x$ materials can be negligible, and the mass of the carbon paper should not be taken into account as active material when we calculated specific capacitance. The area enclosed by CV curve for the porous $Ti_3C_2T_x$ assemblies is obviously larger than that for $Ti_3C_2T_x$ film, which implies that $Ti_3C_2T_x$ assemblies possess bigger areal and specific capacitance. Fig. S3a (Supporting information) shows the galvanostatic charge-discharge (GCD) curves performed at 1 mA/cm^2. The $Ti_3C_2T_x$ assemblies exhibit higher capacitance retention (72.4%) than $Ti_3C_2T_x$ film (43.2%) when the scan rate ranges from 2 mV/s to 50 mV/s, as shown in Fig. S3b (Supporting information), which can attribute to the better ability of ion-diffusion compared with $Ti_3C_2T_x$ film (Fig. S3c in Supporting information). After 5000 cycles, the capacitance retention of $Ti_3C_2T_x$ assemblies is almost the same as that of $Ti_3C_2T_x$ film (Fig. S3d in Supporting information). On the basis of the above results, the superiority of $Ti_3C_2T_x$ assemblies than $Ti_3C_2T_x$ film can be revealed.

In order to explore the impact of mass loadings on capacitance performance, we prepared the $Ti_3C_2T_x$ assemblies electrodes with different mass loadings (1.8, 2.5, 5.3 and 8.4 mg/cm^2). As shown in Fig. 3b, the areal capacitance calculated by integrating the CV curves increases with the loading amount. It is 429.5, 613.3, 1310.0 and 1668.2 mF/cm^2, and the corresponding specific capacitance is 238.6, 245.3, 247.2 and 198.6 F/g, respectively. The superiority of the electrode (5.3 mg/cm^2) is vividly described by Fig. S4 (Supporting information) [32]. The electrode (8.4 mg/cm^2) exhibits the longest discharge time in the GCD curves at 2 mA/cm^2 (Fig. S5 in Supporting information). However, its capacitance rapidly declines as the scan rate increasing (Fig. 3c). The capacitance retention for the electrode (8.4 mg/cm^2) is calculated to be only 28.5%, and the ones for other three electrodes (1.8, 2.5 and 5.3 mg/cm^2) are 74.1%, 71.9% and 49.3%, respectively. It indicates the good rate performance of the electrodes (1.8 and 2.5 mg/cm^2) and the inferior rate capability of the electrodes (5.3 and 8.4 mg/cm^2). To illustrate why the capacitance retention declines so fast as mass loading increases, we carried out EIS measurement in a frequency varying from 10 mHz to 200 kHz. The Nyquist curves in Fig. 3d are similar in form with a quasi-semicircle at the high frequency region and a spike at the low frequency region. The inset is the magnified section in the high frequency. The intercept on the Re(Z) is 0.9, 0.7, 0.9 and 1.1 Ω for 1.8, 2.5, 5.3 and 8.4 mg/cm^2, respectively. It denotes the equivalent series resistance (R_s). Although they are disparate, they are just about 1.0 Ω. The low

R_s indicates the low intrinsic ohmic resistance of the $Ti_3C_2T_x$ assemblies electrodes. In the high-frequency region, the four charge transfer resistances are almost the same and quite small. The Nyquist plots in the low-frequency region exhibit a slope close to 90° along the imaginary axis for the three electrodes (1.8, 2.5 and 5.3 mg/cm^2), while it shows a bigger angle relative to the imaginary axis for the electrode (8.4 mg/cm^2). The slope is related to the diffusive resistance of electrolyte in the electrode pores and the proton diffusion in host materials. The smaller slope for the electrode (8.4 mg/cm^2) should be due to a higher diffusion resistance. Fig. 3e provides a convenient method to show the influence of frequency on imaginary capacitance. It is a quantitative method to weigh how fast the device can be charged and discharged reversibly. The response time is 3.3, 4.2, 11.8 and 30.6 s for the loading mass of 1.8, 2.5, 5.3 and 8.4 mg/cm^2, respectively. It is the reason for the good rate performance of the electrodes (1.8 and 2.5 mg/cm^2) and the inferior rate capability of the electrodes (5.3 and 8.4 mg/cm^2). Generally, high mass loading causes electrolytic ion to diffuse into the active materials difficulty. An increased loading mass induces more active surface areas of the electrodes to lose efficacy at large current densities, which leads to an increased response time [7]. To evaluate cycling stability, the $Ti_3C_2T_x$ assemblies electrode was tested through GCD measurements at 20 mA/cm^2. Its capacitance is maintained 87% of its initial value after 10000 cycles Fig. 3f). The last 5 cycles show a similar symmetrical triangle shape with the first 5 cycles (insets of Fig. 3f), indicating a remarkable cycling stability of the $Ti_3C_2T_x$ assemblies electrodes.

In order to demonstrate the practical application of the porous $Ti_3C_2T_x$ assemblies, supercapacitors were fabricated by using $Ti_3C_2T_x$ assemblies for both positive and negative electrodes, and PVA-H_2SO_4 as electrolyte (Fig. 4a). The CV curves at different scan rates (2∼100 mV/s) for the supercapacitor with the total mass loading of 8.3 mg are shown in Fig. 4b. It should be point out that the total mass loadings here is for the two electrodes of the symmetric solid-state supercapacitors, where mass loadings of positive and negative electrode are equal. The rectangular shape of the CV curves can be well maintained even at a high scan rate of 100 mV/s. Fig. 4c displays the GCD curves of the $Ti_3C_2T_x$-based supercapacitor at different current density (1−20 mA/cm^2). All the curves exhibit perfect linear and symmetrical character, confirming an excellent electrochemical reversibility and a good coulombic efficiency of the $Ti_3C_2T_x$-based supercapacitor. The influence of mass loadings on the electrochemical performance of the $Ti_3C_2T_x$-based supercapacitors is evaluated (Fig. S6 and Table S2 in Supporting information). The power and energy densities of the $Ti_3C_2T_x$-based supercapacitor are compared with other supercapacitors reported previously in Fig. 4d [33–39]. When the power density is 250 μW/cm^2, our $Ti_3C_2T_x$-based supercapacitor exhibits an energy density of 14.7 μWh/cm^2; and when the energy density is 5.8 μWh/cm^2, the power density is 50 mW/cm^2. The $Ti_3C_2T_x$-based solid-state supercapacitors also exhibit good cycling stability (Fig. S7 in Supporting information). To evaluate the potential use in flexible and wearable electronics, a series of comparative experiments under different bending conditions were conducted on the $Ti_3C_2T_x$-based supercapacitors (Fig. S8 in Supporting information). Fig. 4e shows the CV curves under different bending conditions (0°∼135°) at 20 mV/s. No obvious changes of the CV curves are observed, indicating an excellent electrochemical stability of the $Ti_3C_2T_x$-based supercapacitors. To satisfy the actual demands of energy and power, different working windows and prolonged discharging time could be achieved by the series-parallel connection of the $Ti_3C_2T_x$-based supercapacitors. As shown in Fig. 4f, the discharge time of two devices connected in parallel is doubled. Meanwhile, the output voltage of three supercapacitors connected in series is three times as long as that of a single one. In addition, a red light-emitting diode (LED) was lightened by the $Ti_3C_2T_x$-based supercapacitors in series after being charged (Fig. S9 in Supporting information).

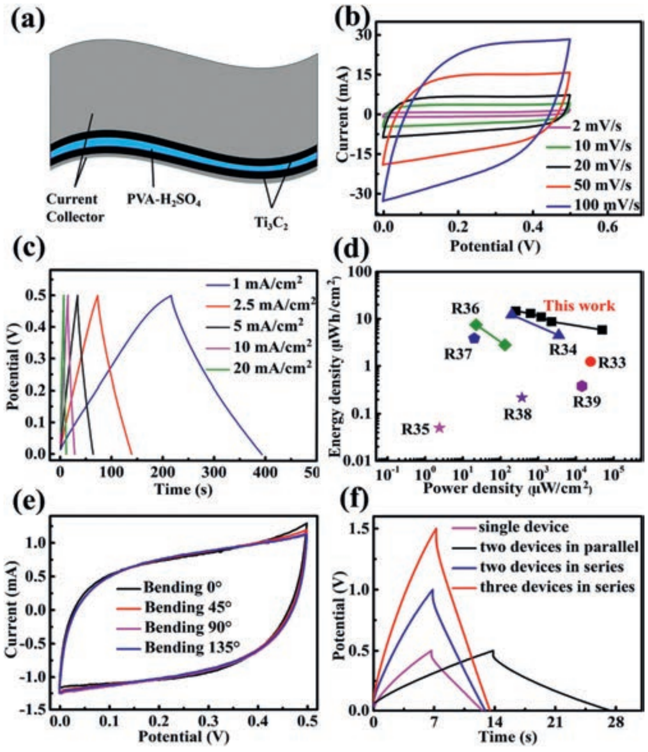

Fig. 4. Electrochemical properties of the flexible symmetric solid-state supercapacitors. (a) Schematic illustration. (b) CV curves. (c) GCD curves. (d) Ragone plots. (e) CV curves carried out at different bent angles. (f) GCD curves of single device, two devices in parallel, and two or three devices in series.

In summary, the three-dimensional porous $Ti_3C_2T_x$ assemblies were synthesized without any additive by introducing ice as spacers, which deliver a maximum areal capacitance (1668 mF/cm^2), an optimized specific capacitance of (247.2 F/g), and excellent capacitance retention (87% after 10000 cycles. In addition, the symmetric solid-state supercapacitors fabricated with the porous $Ti_3C_2T_x$ assemblies exhibit the maximum power density is 50 mW/cm^2. These superior performances might be attributed to the following reasons: (i) the porous network structure; (ii) the larger specific surface area and more electroactive sites; (iii) the more -O terminations. Therefore, the porous $Ti_3C_2T_x$ assemblies are promising candidates for electrochemical energy storage devices.

Declaration of competing interest

The authors claim no conflicts of interest.

Acknowledgments

This work was partially supported by the National Natural Science Foundation of China (Nos. 11504097, 51772069), the Natural Science Foundation of Heilongjiang Province-China (No. QC2017003), and the Scientific Research Foundation of Heilongjiang Province for Returned Chinese Scholars (Wu Lili).

References

[1] X.Y. Shan, N. Zhang, R.D. Zheng, H. Gao, X.T. Zhang, Electrochim. Acta 295 (2019) 286–293.
[2] Y. Liu, P. Zhang, N. Sun, et al., Adv. Mater. 30 (2018) 1707334.

[3] Q. Jin, N. Zhang, C.C. Zhu, H. Gao, X.T. Zhang, Nanoscale 10 (2018) 16935.
[4] R.P. Fang, S.Y. Zhao, Z.H. Sun, et al., Adv. Mater. 29 (2017) 1606823.
[5] V. Strauss, K. Marsh, M.D. Kowal, M. EI-Kady, R.B. Kaner, Adv. Mater. 30 (2018) 1704449.
[6] L.B. Xing, J.L. Zhang, J. Zhang, et al., Electrochim. Acta 176 (2015) 1288–1295.
[7] L. Li, N. Zhang, M.Y. Zhang, et al., ACS Sustain. Chem. Eng. 6 (2018) 7442–7450.
[8] L.L. Liu, Z.Q. Niu, J. Chen, Chin. Chem. Lett. 29 (2018) 571–581.
[9] X.L. Xu, W.H. Shi, W.X. Liu, et al., J. Mater. Chem. A 6 (2018) 24086.
[10] Z.Y. Song, D.Z. Zhu, L.C. Li, et al., J. Mater. Chem. A 7 (2019) 1177–1186.
[11] L. Chen, D.P. Li, L.N. Chen, et al., Carbon 138 (2018) 264–270.
[12] S. Wang, Z.S. Wu, S.H. Zheng, et al., ACS Nano 11 (2017) 4283–4291.
[13] P. Li, W.H. Shi, W.X. Liu, et al., Nanotechnology 29 (2018) 445401.
[14] J.Q. Qin, Z.S. Wu, F. Zhou, et al., Chin. Chem. Lett. 29 (2018) 582–58658.
[15] J.J. Yoo, K. Balakrishnan, J.S. Huang, Nano Lett. 11 (2011) 1423-1142.
[16] Y. Wang, Y.Z. Zhang, D. Dubbink, et al., Nano Energy 49 (2018) 481–488.
[17] N.R. Chodankar, D.P. Dubal, G.S. Gund, C.D. Lokhande, Electrochim. Acta 165 (2015) 338–347.
[18] M. Naguib, M. Kurtoglu, V. Presser, et al., Adv. Mater. 23 (2011) 4248.
[19] J.M. Luo, J.H. Zheng, J.W. Nai, et al., Adv. Funct. Mater. (2019) 1808107.
[20] H. Tang, W.L. Li, L.M. Pan, et al., Adv. Sci. (2018) 1800502.
[21] X.Y. Wang, Q.S. Fu, J. Wen, et al., Nanoscale 10 (2018) 20828–20835.
[22] S.Y. Lin, X.T. Zhang, J. Power Sources 294 (2015) 354–359.
[23] L. Yu, L. Hu, B. Anasori, et al., ACS Energy Lett. 3 (2018) 1597–1603.
[24] H.R. Wang, L. Li, C.C. Zhu, et al., J. Alloys Compd. 778 (2019) 858–865.
[25] X.F. Zhang, Y. Liu, S.L. Dong, J.Q. Yang, X.D. Liu, Appl. Surf. Sci. 485 (2019) 1–7.
[26] L.L. Jiang, Z. Fan, Nanoscale 6 (2014) 1922–1945.
[27] L. Li, M.Y. Zhang, X.T. Zhang, Z.G. Zhang, J. Power Sources 364 (2017) 234–241.
[28] M.M. Hu, T. Hu, Z.J. Li, et al., ACS Nano 4 (2018) 3578–3586.
[29] W.X. Liu, R.L. Yin, X.L. Xu, et al., Adv. Sci. 6 (2019) 1802373.
[30] F.F. Wu, X.B. Gao, X.L. Xu, et al., ChemSusChem 13 (2020) 1537–1545.
[31] Q.S. Fu, J. Wen, N. Zhang, et al., RSC Adv. 7 (2017) 11998–12005.
[32] W.H. Shi, J. Mao, X.L. Xu, et al., J. Mater. Chem. A 7 (2019) 15654.
[33] A. Ramadoss, K.Y. Yoon, M.J. Kwak, et al., J. Power Sources 337 (2017) 159–165.
[34] H.H. Zhou, H.J. Zhi, G.Y. Han, et al., J. Mater. Sci. Mater. Electron. 27 (2016) 2773–2782.
[35] C.F. Zhang, B. Anasori, A. Seral-Ascaso, et al., Adv. Mater. (2017) 1702678.
[36] C.Z. Wei, Q. Xu, Z.Q. Chen, et al., Carbohyd Polym. 169 (2017) 50–57.
[37] L. Kou, T.Q. Huang, B.N. Zheng, et al., Nat. Commun. 5 (2014) 3754.
[38] Y.L. Shao, J.M. Li, A.G. Li, et al., Mater. Horiz. 4 (2017) 1145–1150.
[39] L. Zhang, D.A. Derek, N.T. Alvarez, et al., Small (2017) 1603114.